Crystal Defects in CdZnTe Crystals Grown by the Modified Low-Pressure Bridgman Method

L. Marchini, A. Zappettini, M. Zha, N. Zambelli, A. E. Bolotnikov, *Member, IEEE*, G. S. Camarda, and R. B. James, *Fellow, IEEE*

Abstract—**Cadmium Zinc Telluride (CZT) is among the most promising materials for room-temperature X- and gamma-ray detectors. However, crystal defects such as Te inclusions and subgrain boundaries significantly hamper their performances. In this work, we evaluated CZT crystals grown by the modified low-pressure Bridgman technique at the IMEM Institute, Parma. We characterized the crystals by IR microscopy to identify the sizes and concentrations of the Te inclusions, along with high spatial resolution X-ray response mapping to measure the uniformity of their charge-transport properties. In addition, we employed white X-ray beam diffraction topography to analyze their crystalline structure.**

Index Terms—**CdZnTe, crystal defects.**

I. INTRODUCTION

CdZnTe (CZT) is one of the leading materials used for room-temperature gamma-ray detectors. However, despite its many attractive characteristics CZT crystals contain several types of defects, which play a role in degrading the charge-carrier transport.

Some such defects, like Te inclusions, are related to the growth of CZT crystals from a tellurium-rich melt. Others, like dislocations and subgrain boundaries, result from difficulties in controlling the optimal growth conditions, and from the low thermal-conductivity of CZT.

Identifying defects in CZT material requires several experimental techniques such as IR transmission microscopy and white beam X-ray diffraction topography (WXDT). By correlating non-uniformities in the detector's responses with particular defects and their spatial distributions, we gain an understanding of their influences on the devices' performances.

Recently, at the IMEM Institute in Parma, we grew detector-grade CZT material via the modified low-pressure vertical Bridgman method; the resulting material showed high resistivity and good carrier-transport properties that are well suited to detecting X- and gamma-rays. We detailed these growth experiments in our previous publications [1]–[3]. Here, we discuss our evaluations of these IMEM-grown CZT crystals using several experimental techniques, including X-ray
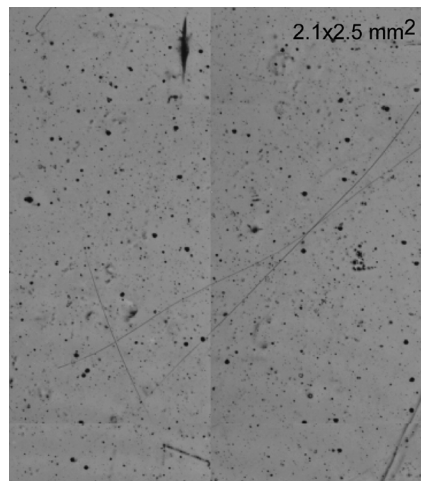
Fig. 1. A 2.1 × 2.5 mm IR-collapsed image of the IMEM samples. The dark dots are Te inclusions with a size of 2- to 30-μm. Some surface scratches due to polishing are apparent.

beams at the National Synchrotron Light Source (NSLS) at Brookhaven National Laboratory.

II. EXPERIMENTAL

We grew eight CZT ingots by the low-pressure Bridgman technique at the IMEM Institute [1]. The CZT polycrystalline charges were synthesized directly from 7N-purity level elements purchased from 5N Plus Inc. After growth, the charge was heated in a high-purity inert gas to improve the stoichiometry of CZT [2]. We optimized the parameters for growing the crystals inside a boron-oxide ampoule via the vertical Bridgman method [3]. The thermal gradient at the growth interface was $\sim 10°$C/cm, and the growth rate was ~ 1 mm/h. The ingots were cooled at $\sim 30°$C/h. We doped the material with indium to induce high electrical resistivity.

Over 20 samples, $7 \times 7 \times 2$ mm^3, were prepared from different locations of the as-grown ingots. The samples' surfaces were polished with diamond paste down to 0.1 μm to remove the damaged layer caused while cutting them. Then, we deposited gold contacts on both surfaces using an aqueous AuCl$_3$ solution. Details of our preparation procedure are given elsewhere [4].

Bulk resistivity was evaluated from fitting the low-voltage region (from -1 to 1 V) of the I-V curve [5]. The spectral responses were measured using standard radiation sources. We evaluated the mobility–lifetime product ($\mu\tau$) for electrons using alpha particle and x-ray-sources; the findings from both methods agreed well.
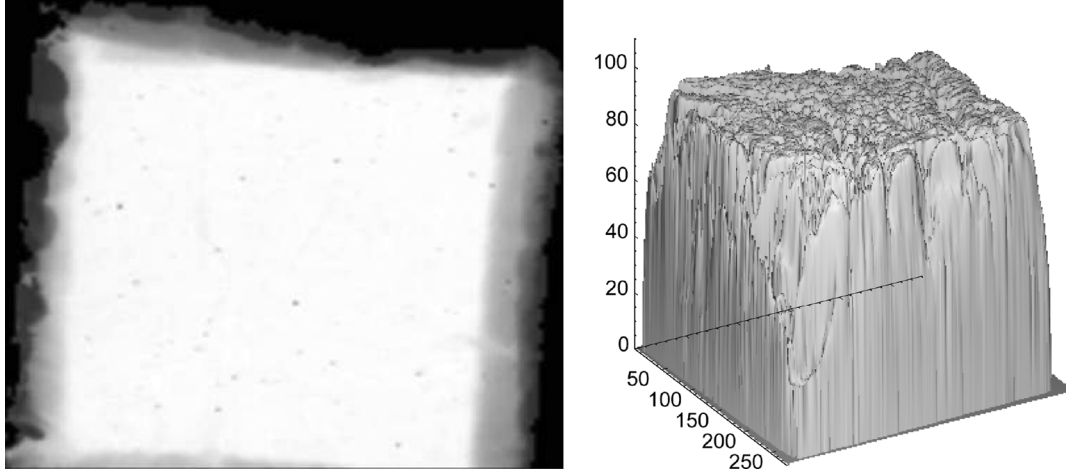
Fig. 2. X-ray response map of an IMEM sample. The resolution of the raster scan is 20 μm, and beam's energy is 25 keV. The right image shows a 3D map of the same sample. The sample's area is about 7 mm × 6 mm, the x and y-axes represent the beam's locations in steps, while the y-axis denotes the signal's amplitudes in channels.

We measured the size distributions and concentration of the Te inclusions, typically present in Te-rich CZT crystals [6], using an IR transmission microscopy system. We used the commercial software packages for processing the IR images. By acquiring a series of images taken at different depths from one side of the crystal to the other (with a step size of 100 microns), we reconstructed a 3D distribution of the Te inclusions. In addition, we generated so-called *collapsed images* by projecting all the inclusions seen in the sample onto a single plane [7], which gave us information on all inclusions in the sample.

These data allowed us to correlate the volumetric distributions of Te inclusions with the non-uniformities of the X-ray response maps measured with a collimated synchrotron X-ray beam as described in [8]. The monoenergetic beam of 24-keV photons impinging on the sample's surface generated an X-ray spectrum at each beam's position. From these spectra, we determined the center of gravity of the peaks, and plotted them as two-dimensional maps. Such maps, normally acquired in 10–100-μm steps, represent the spatial variations of the device's charge collection efficiency.

Finally, we assessed the structural defects in the crystals using WXDT [9], [10]. We took the measurements in a reflection geometry, an extremely versatile technique that allowed us directly to visualize extended defects exiting the crystal's surfaces.

III. RESULTS AND DISCUSSION

The bulk resistivity and electron $\mu\tau$-products, respectively, yielded values of $1\text{–}4 \times 10^{10}$ Ohm · cm and $1\text{–}3 \times 10^{-3}$ cm^2/V. The IR measurements revealed the presence of 2- to 30-μm Te inclusions at a concentration of about 6×10^5 cm^{-3}. Fig. 1 shows an example of a representative collapsed IR image. The dark spots are Te inclusions; some scratches from polishing are also visible.

The image in Fig. 2 (left) illustrates the high uniformity of the X-ray response map obtained for another sample; the pulse-height histogram of these distributions give a narrow peak with a FWHM of <2%. The bright background in the map represents
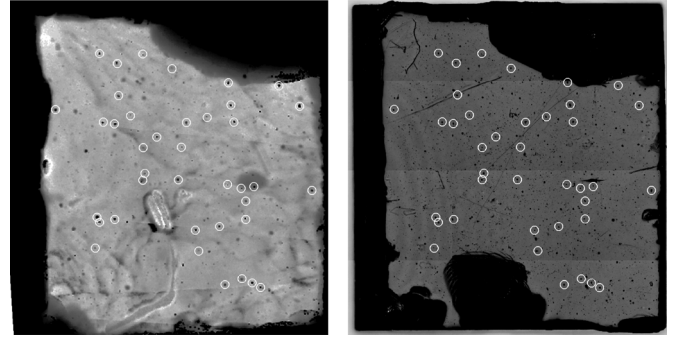

Fig. 3. Correlation between the X-ray response map (left) and the IR collapsed image (right) over the entire area of the sample (7 mm × 6 mm). In both maps, the Te inclusions are circled in white. The big dark spots are regions where the sample surface was chipped during the measurements.

the response of a good detector; the dark spots correspond to regions exhibiting deteriorated efficiency in charge collection. On average, this detector showed good charge-collection efficiency, as is evident from the 3D map image in Fig. 2 (right).

Fig. 3 reveals the correlations between the X-ray response map (left) and the IR image (right). Many Te inclusions (encircled) in the IR image correspond with the dark spots (also encircled) in the X-ray response map. These reciprocal relationships demonstrate that Te inclusions are responsible for the deterioration of the device's response, as previously demonstrated [11].

We note, however, that many inclusions in the IR image do not have counterparts in the X-ray response map. This discrepancy reflects the important roles of diffusion and electrostatic repulsion of the electrons in the clouds as they drift from the cathode to the anode. Inclusions located near the cathode trap a greater fraction of charge from the electron cloud, while the deep inclusions interact with much larger electron clouds, and thus, they trap lesser amounts of the charge. For the same reason, smaller inclusions that are visible in the IR image are barely seen in the X-ray response map.

To illustrate these interplays, Fig. 4 shows the correlations between the Te inclusions located near the anode's surface and
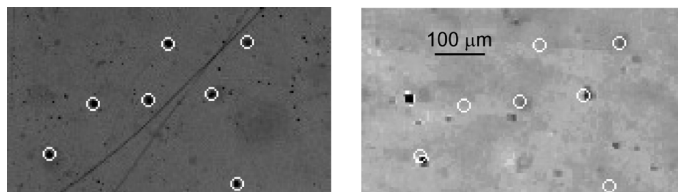
Fig. 4. IR transmission image (left) from the region near the anode and X-ray response map (right) taken for an IMEM sample. The diameters of the circled inclusions are 15–20 μm. Only a few of the inclusions identified in the IR image are evident in the X-ray response map.
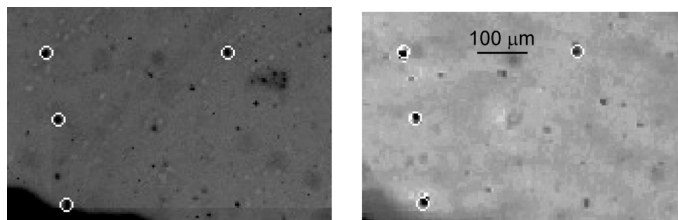

Fig. 5. X-ray response map (right), and the IR top image (left) of an IMEM sample. The diameters of the encircled inclusions are 15–20 μm. Many such correlations were observed in this region of the sample.
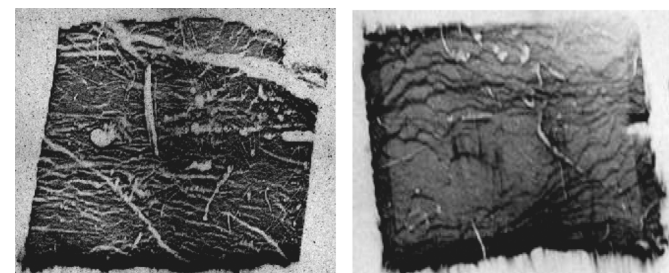

Fig. 6. White beam X-ray diffraction topography (WXDT) images of two representative samples with subgrain boundaries. The sample's areas were 7×7 mm^2.
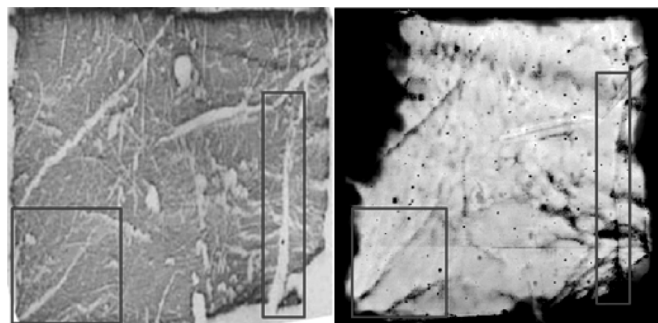

Fig. 7. Correlation between the white beam X-ray diffraction topography (WXDT) image on the left and the X-ray response map on the right. The rectangles show areas containing extended defects wherein charge-collection efficiency is lowered. The sample's sizes were 7×7 mm^2.

map. Such deterioration inevitably is associated with subgrain boundaries [12], [13].

IV. CONCLUSIONS

We evaluated CZT material, grown by the low-pressure vertical Bridgman technique at IMEM, demonstrating its high resistivity at room temperature, its large electron $\mu\tau$-product, and its good uniformity in response, so confirming its suitability for thin radiation detectors (up to 5 mm) used in medical and radiography applications.

The bulk resistivity and the electron $\mu\tau$-products were evaluated in over 20 samples yielding values of $\sim 3 \times 10^{10}$ Ohm $\cdot$ cm and $\sim 10^{-3}$ cm^2/V, respectively.

We acquired X-ray response maps with a highly collimated X-ray beam at BNL's NSLS. The detectors' responses exhibited high uniformity with an FWHM of the response function of $<2\%$.

Several improvements are needed, primarily related to reducing the sizes and concentrations of Te inclusions and subgrain boundaries.

We confirmed the presence of Te inclusions in the as-grown material by IR transmission microscopy, and directly correlated their positions with the charge-collection efficiency maps; a strong correlation was apparent for large inclusions (15–20 μm) lying near the cathode region. In addition, we correlated the small inclusions (8–10 μm) therein with the X-ray-response map.

The X-ray diffraction topography was carried out in a reflection geometry mode. The correlation between the X-ray response maps and diffraction topographs allowed us to assign a role to the extended defects in the deterioration of the detector's response; a large number of subgrain boundaries, evident in the X-ray topography images, was also found to greatly lower this response.

X-ray response map. In fact, only three large Te inclusions have correlated features in the x-ray response map.

In contrast, Fig. 5 shows that all the big inclusions in the X-ray response map have their counterparts in the IR image from the region near the cathode's surface. This finding signifies that the deterioration of the detector's response caused by Te inclusions strongly depends on the position of such inclusions with respect to the location of the interaction point, or to the electron cloud's drift distance.

Several other features appear in the X-ray diffraction topography image, as is evident in Fig. 6(a) and (b). The black and white lines in Fig. 6(a) correspond to subgrain boundaries encompassing different concentrations of dislocations. These are typical of the defects observed in low-pressure Bridgman CZT crystals grown at IMEM. The white lines in the topographs in Figs. 6 and 7 represent subgrain boundaries filled with a high density of dislocations lying perpendicular to the samples' surfaces. Our interpretation is confirmed by the lack of diffraction from those close to polycrystalline areas.

Fig. 7 depicts the correlation between the X-ray response map and the X-ray diffraction topograph of the same sample. The subgrain boundaries identified in the diffraction topography images correspond to the degraded areas in the X-ray response

REFERENCES

[1] A. Zappettini, L. Marchini, M. Zha, G. Benassi, N. Zambelli, D. Calestani, L. Zanotti, E. Gombia, R. Mosca, M. Zanichelli, M. Pavesi, N. Auricchio, and E. Caroli, "Growth and characterization of CZT crystals by the vertical Bridgman method for X-ray detector applications," *IEEE Trans. Nucl. Sci.*, vol. 58, pp. 2352–2356, 2011.

[2] M. Zha, F. Bissoli, A. Zappettini, G. Zuccalli, L. Zanotti, and C. Paorici, "Heat treatment in semi-closed ampoule for obtaining stoichiometrically controlled cadmium telluride," *J. Crystal Growth*, vol. 237, pp. 1720–1725, 2002.

[3] M. Zha, A. Zappettini, D. Calestani, L. Marchini, L. Zanotti, and C. Paorici, "Full encapsulated vertical Bridgman method," *J. Crystal Growth*, vol. 310, pp. 2072–2075, 2008.

[4] L. Marchini, A. Zappettini, E. Gombia, R. Mosca, and M. Lanata, "Study of surface treatment effects on the metal-CdZnTe interface," *IEEE Trans. Nucl. Sci.*, vol. 56, pp. 1823–1826, 2009.

[5] M. Prokesch and C. Szeles, "Accurate measurement of electrical bulk resistivity and surface leakage of CdZnTe radiation detector crystals," *J. Appl. Phys.*, vol. 100, pp. 014503–01409, 2006.

[6] T. E. Schlesinger, J. E. Toney, H. Yoon, E. Y. Lee, B. A. Brunett, L. Franks, and R. B. James, "Cadmium zinc telluride and its use as a nuclear radiation detector material," *Mater. Sci. Eng. Reports*, vol. 32, pp. 103–189, 2001.

[7] R. J. Pieper and A. Korpel, "Image processing for extended depth of field," *Appl. Opt.*, vol. 22, pp. 1449–1453, 1983.

[8] G. A. Carini, A. E. Bolotnikov, G. S. Camarda, and R. B. James, "High-resolution X-ray mapping of CdZnTe detectors," *Nucl. Instr. Meth. A*, vol. 579, no. 1, pp. 120–124, 2007.

[9] A. Authier, S. Lagomarsino, and B. K. Tanner, "X-ray and neutron dynamical diffraction," *NATO ASI Series B*, vol. 3571996, 1996.

[10] G. S. Camarda, A. E. Bolotnikov, Y. Cui, A. Hossain, S. A. Awadalla, J. Mackenzie, H. Chen, and R. B. James, "Polarization studies of CdZnTe detectors using synchrotron X-ray radiation," *IEEE Trans. Nucl. Sci.*, vol. 55, pp. 3725–3730, 2009.

[11] G. A. Carini, A. E. Bolotnikov, G. S. Camarda, G. W. Wright, R. B. James, and L. Li, "Effects of Te precipitates on the performance of CdZnTe detectors," *Appl. Phys. Lett.*, vol. 88, pp. 143515–143526, 2006.

[12] H. F. Matare, *Defects Electronics in Semiconductor*. New York: Wiley-Interscience, 1971.

[13] A. E. Bolotnikov, S. O. Babalola, G. S. Camarda, H. Chen, S. Awadalla, Y. Cui, S. U. Egarievwe, P. M. Fochuk, R. Hawrami, A. Hossain, J. R. James, I. J. Nakonechnyj, J. Mackenzie, G. Yang, C. Xu, and R. B. James, "Extended defects in CdZnTe radiation detectors," *IEEE Trans. Nucl. Sci.*, vol. 56, pp. 1775–1783, 2009.